

# Deep Fusion Prior for Multi-Focus Image Super Resolution Fusion

Yuanjie Gu, Zhibo Xiao, Hailun Wang, Cheng Liu, and Shouyu Wang

*Computational Optics Laboratory, School of Science, Jiangnan University, Wuxi, Jiangsu 214122, China*

*({yuanjie\_gu; zhibo\_xiao; hailun\_wang}@stu.jiangnan.edu.cn, chengliu@siom.ac.cn, shouyu@jiangnan.edu.cn)*

**Abstract**—This paper unifies the multi-focus images fusion (MFIF) and blind super resolution (SR) problems as the multi-focus image super resolution fusion (MFISRF) task, and proposes a novel unified dataset-free unsupervised framework named deep fusion prior (DFP) to address such MFISRF task. DFP consists of SKIPnet network, DoubleReblur focus measurement tactic, decision embedding module and loss functions. In particular, DFP can obtain MFISRF only from two low-resolution inputs without any extent dataset; SKIPnet implementing unsupervised learning via deep image prior is an end-to-end generated network acting as the engine of DFP; DoubleReblur is used to determine the primary decision map without learning but based on estimated PSF and Gaussian kernels convolution; decision embedding module optimizes the decision map via learning; and DFP losses composed of content loss, joint gradient loss and gradient limit loss can obtain high-quality MFISRF results robustly. Experiments have proved that our proposed DFP approaches and even outperforms those state-of-art MFIF and SR method combinations. Additionally, DFP is a general framework, thus its networks and focus measurement tactics can be continuously updated to further improve the MFISRF performance. DFP codes are open source and will be available soon at <http://github.com/GuYuanjie/DeepFusionPrior>.

**Index Terms**—Multi-focus image fusion, super resolution, unified model, unsupervised learning, dataset-free learning

## 1 Introduction

The majority of information acquisition, processing and analysis are based on visual perception system, which first records images, then distinguishes, recognizes and extracts targets, and finally analyzes them to provide instructions for system decision and control. Among them, image recording is the key premise for precision decision; but unfortunately, due to depth of field (DoF) and resolution limitations of optical systems, recorded images often suffer from resolution reduction and defocus blur, thus inevitably deteriorating the subsequent image processing and analysis. Therefore, in order to improve image quality, multi-focus image fusion (MFIF) and super-resolution (SR) methods have been adopted to extend the imaging DoF and enhance the imaging resolution, respectively.

For MFIF, methods can be roughly divided into two categories according to whether or not using deep learning. Most non-deep learning methods determine focus measurements and obtain decision maps to guide fusion [4], [5], [6]. However, these decision maps suffer from disadvantages such as edge fragmentation and obvious transition. Supervised deep learning methods can obtain high-quality decision maps [22], [23], [24] but they rely on large handcrafted datasets. Unsupervised deep learning methods transform ground truths to features which can be obtained from inputs [28], [29]. Nevertheless, most of these features excessively rely on gradient, often leading to image edge deepening and painterly stylization. Besides, these unsupervised methods still require large datasets. For SR, interpolation, example and deep learning approaches are commonly used. Interpolation approaches only use pixel information of low-resolution image itself to interpolate pixel based on its surrounding, but their reconstruction results are often blurry. Example methods learn mapping between low- and high-resolution patches from internal or external datasets [37], [40], while the feature extraction and mapping functions are still handcrafted, which inevitably limit high-frequency information learning. Supervised deep learning approaches reconstruct high-frequency information or fuse multi-scale information for resolution improvement [54], [55]; while unsupervised ones enhance resolution via generative adversarial game or iteration [60], [64]. Moreover, almost all the works deal with MFIF and SR separately, however, we find that MFIF and SR share a unified physical model. The imaging process can be described as

$$i(x, y) = h(x, y) * o(x, y) + n(x, y) \quad (1)$$

where  $h(x, y)$  is the 2-D point spreading function (PSF),  $o(x, y)$  is the object,  $n(x, y)$  is the additive noise,  $*$  is the spatial convolution, and  $i(x, y)$  is the image. For SR, its purpose is to use  $i(x, y)$  to obtain an estimate  $\hat{o}(x, y)$  of the real object  $o(x, y)$ . While for MFIF, its model can be described in Eq. (2), where  $i_f(x, y)$  and  $i_b(x, y)$  are the unfused images focusing on foreground and background,  $m_f(x, y)$

and  $m_b(x,y)$  are the decision maps determining the foreground and background regions,  $E$  is the identity matrix, and  $u(x,y)$  is the fused image.

$$u(x, y) = m_f(x, y) \cdot i_f(x, y) + m_b(x, y) \cdot i_b(x, y) \quad (2a)$$

$$m_f(x, y) + m_b(x, y) = E \quad (2b)$$

Both  $i_f(x,y)$  and  $i_b(x,y)$  can be represented by Eqs. (3a) and (3b), in which  $o_f(x,y)$  and  $o_b(x,y)$  are the foreground and background objects, and  $h_f(x,y)$  and  $h_d(x,y)$  are the 2-D focus and defocus PSFs.

$$i_f(x, y) = h_f(x, y) * o_f(x, y) + h_d(x, y) * o_b(x, y) + n_f(x, y) \quad (3a)$$

$$i_b(x, y) = h_d(x, y) * o_f(x, y) + h_f(x, y) * o_b(x, y) + n_b(x, y) \quad (3b)$$

Eq. (4) can be obtained by substituting Eq. (3) into Eq. (2a), and it can be further generalized to Eq. (5).

$$\begin{aligned} u(x, y) = & \left\{ \left[ m_f(x, y) \cdot h_f(x, y) + m_b(x, y) \cdot h_b(x, y) \right] * o_f(x, y) \right. \\ & + \left[ m_f(x, y) \cdot h_d(x, y) + m_b(x, y) \cdot h_f(x, y) \right] * o_b(x, y) \left. \right\} \\ & + m_f(x, y) \cdot n_f(x, y) + m_b(x, y) \cdot n_b(x, y) \end{aligned} \quad (4)$$

$$u(x, y) = \hat{h}(x, y) * o(x, y) + \hat{n}(x, y) \quad (5)$$

According to Eqs. (2) to (5), for MFIF, its purpose is to use  $i_f(x,y)$  and  $i_b(x,y)$  to obtain the  $\hat{o}(x,y)$  for image fusion. Therefore, it reveals that MFIF and SR share the unified physical model, and MFIF and SR are belong to a one-stage ill-posed inverse problem.

Here, we propose deep fusion prior (DFP), which implements MFIF and blind SR with unified, unsupervised, dataset-free and robust model. DFP consists of our designed DoubleReblur as a focus measurement method to determine focus region and obtain decision map and a generative autocoder network SKIPnet to reconstruct fused super resolution image. The core idea of DoubleReblur is to reblur the image via kernel convolution: the clear focus region becomes blurred, and the defocus region is still blurred. Therefore, the focus region can be determined according to difference between the reblurred and original images. Moreover, in order to enhance the performance, the estimated PSF kernel and Gaussian kernel are used to double reblur. Based on the DoubleReblur determined focus regions, decision map can be obtained using the largest region floorfill algorithm. The SKIPnet iteratively updates the parameters with invariable input, and the fused super resolution image is generated using the loss functions to constrain solution space. The designed loss functions are composed of content loss and joint gradient loss: the content loss is to constrain the SKIPnet to learn the clear region of each image; while the joint gradient loss is to enhance the SKIPnet to learn the high frequency information and to reduce the dependency of decision maps. The selectable learning-based map embedding can be used to optimize the performance of the decision maps. Foremost, the main contributions of the proposed DFP are summarized as follows:

- *In theory*, we unify the MFIF and SR problems as a **MFISRF** problem to propose a new perspective for MFIF and SR.
- *In framework design*, we propose a **unified, dataset-free, unsupervised** and **robust** framework DFP to address the MFIF and SR problems based on their unified model. The DFP works with only one network for MFIF and SR. It is an unsupervised method without ground truth. The fusion performance does not completely rely on the quality of the obtained decision maps. Additionally, the DFP is a generic framework, so the network architecture and focus measurement method are replaceable.
- *In performance testing*, we compare our DFP with the combinations of 12 deep learning based MFIF methods and 3 SR methods on the latest MFI-WHU [1] benchmark dataset. The adopted 12 deep learning based MFIF methods include 6 supervised methods and 6 unsupervised methods, almost covering the state-of-art deep learning based MFIF methods. Moreover, the adopted 3 SR methods include conventional method, unsupervised deep learning based method and supervised deep learning base method.

The paper is organized as follows: first, we review the related works on MFIF and SR in Section 2; then, we introduce the details of DFP in Section 3; next, we test the performance of DFP via comparing other reported works in Section 4; and finally, we discuss and conclude this work in Sections 5 and 6, respectively.

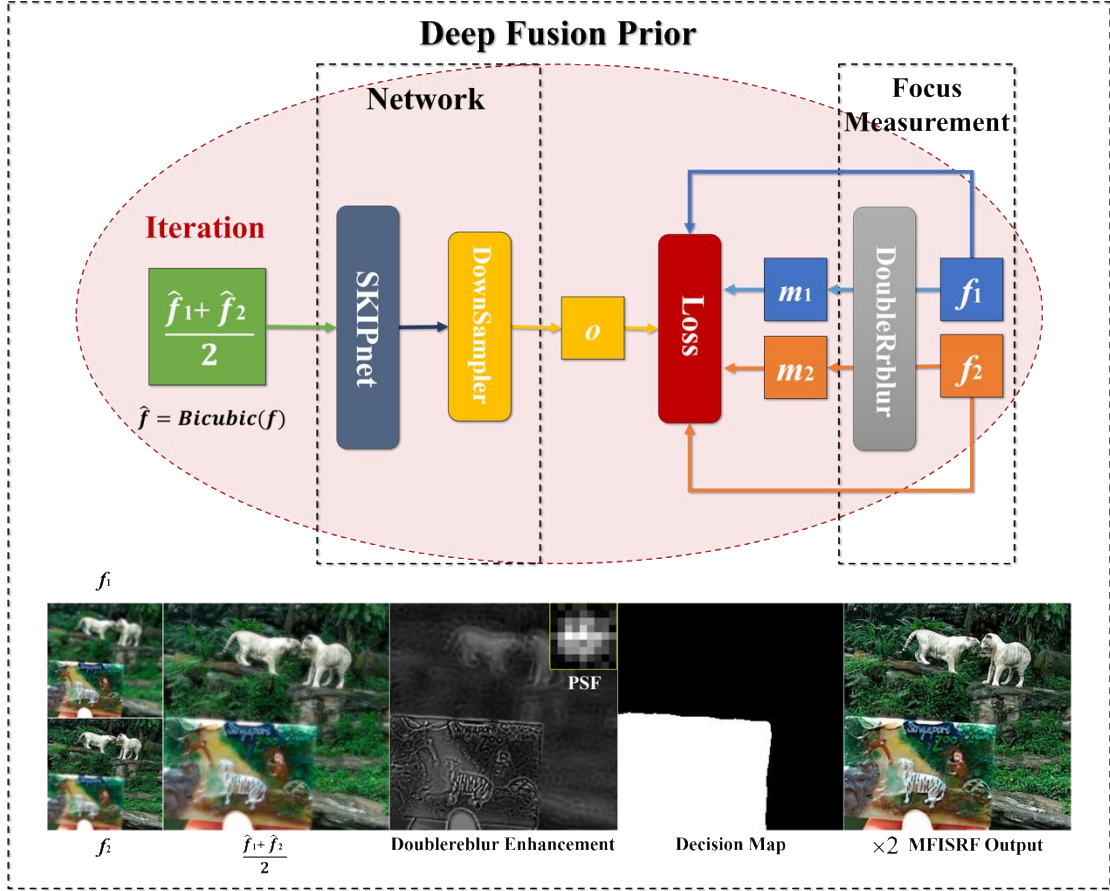


Fig. 1. Schematic illustration of our DFP and some examples.

## 2 Related Works

### 2.1 MFIF Methods

For MFIF, methods can be classified into non-deep learning and deep learning types. In non-deep learning approaches, MFIF can be roughly summarized as an inverse process of extraction, and the key to these approaches lies in two important aspects: focus measurement and fusion rules. MFIF focus measurement can be implemented in either spatial domain or transform domain. There are mainly 3 tactics in focus measurement in spatial domain such as pixel- [2], [3], [4], [5], [6], [7], [8], block-[9] and region-based ones [10]. Pixel-based methods implement focus measurement via mean filter, guided filter, cross bilateral filter and dense scale invariant feature transform, etc. In block-based focus measurement method such as quadtree-based algorithm, it decomposes image into blocks with optimal sizes to compute focus measurement weight, and reconstructs fusion image from blocks. The region-based focus measurement method such as boundary finding based algorithm tracks the boundaries between the focus and defocus regions. Although spatial domain methods can obtain focus measurement, these methods are not generalizable enough, focus measurement approaches in transform domain can improve the performance. There are mainly 5 tactics in focus measurement in transform domain such as sparse representation-based [11], [12], multi-scale-based [13], [14], [15], [16], [17], gradient-based [18], [19], feature-space-based [20] and hybrid ones [21]. Sparse representation-based methods implement focus measurement via adaptive sparse representation model, thus solve the disadvantages of patches sampling by convolutional sparse representation. Multi-scale-based methods obtain more accurate focus measurement via wavelet transform, adaptive segmentation, singular value decomposition (SVD), energy of Laplacian, guided filtering and weighted guided filtering, etc. In order to enhance the high frequency information, gradient-based methods are developed for color images to obtain the fused luminance using such as Haar wavelet-based image reconstruction based on blending the gradients of the luminance components of the input images using the maximum gradient magnitude at each pixel location. Feature-space-based methods realize focus measurement via sparse feature matrix decomposition and morphological filtering. Hybrid methods combine these above methods to improve the focus measurement performance. However, these transform domain methods are mostly based on Laplacian pyramid, gradient pyramid, discrete wavelet (DWT), discrete cosine (DCT), curvelet

transform (CVT) and so on. These handcrafted focus measurement approaches make fusion methods increasingly complex, thus intensifying the difficulty of designing fusion rules. Meanwhile, these handcrafted focus measurement approaches also cause edge fragmentation, obvious transition and many other problems. Besides, the fusion rules are determined based on focus measurement. The often used rules include maximum, minimum, addition, l1-norm, and so on. However, the limit choices of these handcrafted fusion rules produce a glass ceiling on the performance improvement even in some CNN-based methods.

Learning-based MFIF can often obtain end-to-end fusion, since they use networks act as fusion rules. There are mainly two categories as supervised learning-based and unsupervised learning-based approaches. The supervised learning methods include CNN [22], DRPL [23], ECNN [24], IFCNN [25], MADCNN [26] and PCANet [27]. CNN is the first learning-based model realizing end-to-end MFIF: focus measurement and fusion rule can be jointly generated through learning a CNN model, therefore it overcomes the difficulty in the conventional MFIF methods. Subsequently, a series of CNNs are used in MFIF. IFCNN extracts and fuses features from multiple inputs to achieve feature reconstruction. MADCNN is a deep convolutional network based on multi-scale feature extraction unit to implement fusion. DRPL is a deep regression pair learning network which converts the whole image into a binary mask without any patch operation. PCANet is a very simple deep learning model to extract image features but still has good fusion performance. Furthermore, ECNN proposes an ensemble learning method to improve the fusion performance based on combinations of different CNNs. Although these supervised methods have good performance in MFIF, they highly rely on large handcrafted datasets. However, handcrafted datasets often fail in real-world applications. The unsupervised learning methods including FusionDN [28], GCF [29], SESF [30], MFF-GAN [1], PMGI [31] and U2Fusion [32]. FusionDN is an unsupervised and unified network for different fusion tasks, and U2Fusion is its upgraded version. GCF is an unsupervised model based on gradient and connected region. SESF is an unsupervised autocoder network based on spatial frequency and gradient. MFF-GAN is a generative adversarial network with adaptive and gradient joint constraints. PMGI is a fast and unified image fusion network based on proportional maintenance of gradient and intensity. However, because most of these methods often try to sharpen the edges via object enhancement and gradient, the difference between fused image and ground truth is still significant. Besides, almost all of these methods rely on large datasets to drive.

## 2.2 SR Methods

For SR, methods can be classified into interpolation-based, example-based and deep learning-based types. In these approaches, SR can be summarized as an ill-posed inverse process of imaging. The interpolation-based methods rely on sampling and interpolating, and these interpolating tactics include nearest-neighbor, bilinear, bicubic, Sinc, Lanczos and so on. These interpolation-based methods only use the pixel information of low-resolution image itself, and the pixel at each position is interpolated based on the information around the pixel, so the reconstructed images are significantly blurry.

The example-based methods exploit transposed convolution [33], [34], sub-pixel [35] or meta upscale [36] to learn the mapping between the low-resolution and high-resolution patches from internal or external datasets. For example-based SR with internal datasets, [37], [38], [39], [40] exploit the self-similarity property in natural images and construct low-resolution and high-resolution patch pairs based on multi-scale pyramid. Although these internal dataset-based methods [37], [38], [39] can improve the quality, it is difficult to learn high frequency information and large textural variations, and significantly slow to learn; moreover, the generating reconstruction images often have marked serration. Therefore, external dataset-based methods [40] are used to replenish high frequency from external images. Although these methods are efficient, the feature extraction and mapping functions are handcrafted, which limit high frequency information learning.

In order to overcome the limitations of above approaches, deep learning-based approaches are proposed. There are mainly two categories as supervised learning-based and unsupervised learning-based approaches. Since Dong et al. [42SRCNN] pioneered the first supervised deep learning-based single image SR approach, a lot of end-to-end CNNs [42], [43], [44], [45], [46], [47] have been designed to improve the SR quality, and the key to these approaches lies in two important aspects: network backbone and upsampling order. For network backbone design, LeNet [48] and AlexNet [49] are the early works. Since VGG [50] and GoogLeNet [51] were proposed, very deep networks and multi-scale fusion networks have been adopted in SR [52]. With the proposing of ResNet [53] and DenseNet [54], more residual blocks, dense blocks and residual dense blocks (RDB) are used to increase gradients and flow of information in SR [46], [47]. For upsampling order design, these methods can be divided into pre-upsampling SR, post-upsampling SR, progressive upsampling SR and iterative up-and-down sampling SR [57]. Because it is difficult to learn the mapping between low- and high-dimensional spaces, the pre-upsampling SR methods [41], [58] are proposed by upsampling the low-resolution images using conventional interpolation and refining them using networks. But pre-upsampling methods often introduce noise amplification

and blurring. In order to maximize the characteristics of deep learning, post-upsampling SR methods [44], [45], [46] are proposed by upsampling the low-resolution images using learnable upsampling layers at the end of the network. These methods can reduce the computation consumption and spatial complexity. Therefore, post-sampling is the most popular upsampling order. In order to simplify the learn complexity, progressive upsampling SR methods [43], [57] are proposed to reconstruct higher quality SR images using cascade of CNNs. Iterative up-and-down sampling SR methods [58], [59] are designed to better capture mutual dependency between low-resolution and high-resolution images, thus can also be used to capture context from images sequence to learn better feature representations. Almost all of these supervised deep learning based approaches rely on the large datasets consisting of fixed-system low-resolution and high-resolution images pairs. Unsupervised SR approaches are mainly based on adversarial generative networks [60], [61], [62], thus they are not fully unsupervised and rely on large datasets. Deep-image-prior [64] (DIP) shows that the structure of a generator deep neural networks is sufficient to capture a great deal of image statistical prior. It only needs low resolution image as inputs to reconstruct high resolution image at any scale. Like TV norm [63], DIP is effectively handcrafted prior. It is fully unsupervised without any external datasets and performs well dealing with textured and focused goals, although, not well for defocus goals.

Up to now, there is still no unified model that can implement both SR and MFIF tasks with only one network. Besides, almost all of the supervised and unsupervised deep learning-based methods except DIP require large datasets for training in both SR and MFIF tasks. Therefore, according to our unified MFIF and SR model explained in Eqs. (2) to (5), a unified, dataset-free and unsupervised method for MFIF and SR should be considered.

### 3 Deep Fusion Prior Model

In this section, we introduce the details of our proposed DFP model. Based on our unified MFIF and SR model, we introduce the unsurprised DFP model consisting of SKIPnet, DoubleReblur, decision embedding and loss functions in the DFP.

#### 3.1 Unsupervised DFP model

From a Bayesian perspective, either MFIF or SR problem can be represented by Eq. (6)

$$\hat{o}(x, y) = \arg \max_{o(x, y)} \log p[u(x, y) | o(x, y)] + \log p[o(x, y)] \quad (6)$$

where  $\log p(u/o)$  represents the log-likelihood of observation  $u$ ,  $\log p(o)$  furnishes the prior of real scene independently. Furthermore, Eq. (6) can also be formulated as the energy minimization function as follows:

$$\hat{o}(x, y) = \arg \min_{o(x, y)} \frac{1}{2\sigma^2} \|u(x, y) - \mathcal{T}[o(x, y)]\|^2 + \lambda \mathcal{R}[o(x, y)] \quad (7)$$

where  $\frac{1}{2\sigma^2} \|u(x, y) - \mathcal{T}[o(x, y)]\|^2$  is a data term, and  $\lambda \mathcal{R}[o(x, y)]$  is a regularization term with regularization parameter  $\lambda$ .

Specifically, the data term guarantees the solution accords with the degradation process, while the prior term alleviates the ill-posedness by enforcing desired property on the solution.

Generally, the supervised learning-based methods to solve Eq. (7) train an optimization of a loss function in a dataset composed of N “single image super resolution as HR-LR  $\{(y_i, x_i)\}_{i=1}^N [x], [x], [x], [x]$ ”, “multi-images super resolution as HR-LRs  $\{(y_i, (x_{1i}, x_{2i}, \dots, x_{ni}))\}_{i=1}^N [x], [x], [x], [x]$ ” and “multi-focus fusion as fused-unfused  $\{(y_i, (x_{1i}, x_{2i}, \dots, x_{ni}))\}_{i=1}^N [x], [x], [x], [x]$ ” image pairs. For “HR-LR”, the training process can be represented as Eq. (8a); while for “HR-LRs” and “fused-unfused” tasks, the training process can be represented as Eq. (8b).

$$\min_{\Theta} \sum_{i=1}^N \mathcal{L}(\hat{x}_i, x_i) \quad (8a)$$

$$\min_{\Theta} \sum_{i=1}^N \mathcal{A}[\hat{x}_i, (x_{1i}, x_{2i}, \dots, x_{ni})] \quad (8b)$$

where  $\Theta$  is the trainable parameters, and  $\mathcal{L}$  is the loss function.

It is easy to note that “HR-LRs” task is similar to “fused-unfused” task. The difference between them is the label  $\hat{x}_i$ , which limits the solution space of the model.

Furthermore, the unsupervised learning-based methods to implement the “HR-LRs” and “fused-unfused” task is to model rules  $\tau$  for converting inputs  $(x_{1i}, x_{2i}, \dots, x_{ni})$  to label  $\hat{x}_i$ .

However, the ground truth of the real scene is impossible to obtain directly. Therefore, from what has been discussed above, we can unify the MFIF and SR as follows:

$$\min_{\Theta} \sum_{i=1}^N \mathcal{L}[\tau(x_{1i}, x_{2i}, \dots, x_{ni}), (x_{1i}, x_{2i}, \dots, x_{ni})] \quad (9)$$

### 3.2 Deep Fusion Prior Framework

According to Eq. (9), we proposed the DFP to implement MFISRF without any dataset. Furthermore, we formulated the MFISRF task as the unified unsurprised dataset-free task with Eq.(10).

$$\min_{\Theta} \sum_{i=1}^K \mathcal{L}[\tau(x_1, x_2, \dots, x_n), n] \quad (10)$$

where  $n$  is the random noise or the average of the interpolations,  $x_1, x_2, \dots, x_n$  are the low resolution multi-focus images inputs,  $\tau$  is the focus measurement tactic and  $K$  is the number of iterations.

To solve the training optimization problem on Eq. (10), the SKIPnet which based on the encoder-decoder architecture is adopted as the generator network. The DFP details are shown on Fig. 1, and its core ideas are summarized as follows:

- With the multi-channel 2D random noise or the average interpolated low-resolution images as input, the high-quality MFISRF image is finally generated relying on the handcrafted focus measurement and the SKIPnet acting as fusion rules.
- For focus measurement, we proposed DoubleReblur based on computational imaging, morphological image processing and graphics without learning.
- In order to optimize the decision map obtained by handcrafted designed DoubleReblur, we proposed the **learning-based** decision embedding module. The decision embedding module is not indispensable, but the DFP performance will be better with it.
- Utilizing the optimized decision maps, we designed loss function composed of content loss and joint gradient loss to obtain high-quality MFISRF results through iterations.

For the whole DFP, we use Algorithm 1 to describe it.

<b>Algorithm 1</b> Deep Fusion Prior	
1:	Input: foreground input $i_{fore}$ , background input $i_{back}$
2:	<b>DoubleReblur</b> ( $i_{fore}, i_{back}$ )
3:	<b>Decision Embedding</b>
4:	<b>for</b> iterations $K=1000$ <b>do</b>
5:	Forward: $\hat{i}_{MFISRF} = \mathbf{SKIPnet}(\text{input } n)$ ;
6:	Select LANCZOS2 to downsample $\hat{i}_{MFISRF}$ ;
7:	$\mathcal{L} = \mathcal{L}_{con} + 0.5 \cdot \mathcal{L}_{j\_grad} + 0.1 \cdot \mathcal{L}_{grad}$ ;
8:	Backward to update SKIPnet parameters $\Theta$ ;
9:	<b>end for</b>
10:	Output $\hat{i}_{MFISRF}$ .

However, DFP is a robust generic framework. The focus measurement and SKIPnet are replaceable, the MFISRF results can be improved via using updated focus measurement and networks.

#### 3.2.1 SKIPnet Architecture

It is well-known that the encoder-decoder framework is effective for generative works. In addition, U-Net [65] structures have been proved excellent for tasks such as image generation and segmentation. However, in order to guarantee the image-to-image translation invariance, there is no padding before convolution in U-Net. Because of this, the shape between input and output is imparity. Moreover, this imparity also impacts the feature concatenation. While the input in SKIPnet is a random noise or the average

interpolated low-resolution images, the generative relation between input and output is more important than translation invariance. Therefore, reflection paddings and  $1 \times 1$  convolutions are adopted to keep the shape of feature map fixed. Leaky-ReLU activation function is also used to enhance the effect. Note that this work focuses on proposing a powerful and flexible unsupervised MFISRf method without any dataset rather than proposing new generator network architecture. As a matter of fact, the similar architectures of autocoder network can be found in [64], [66].

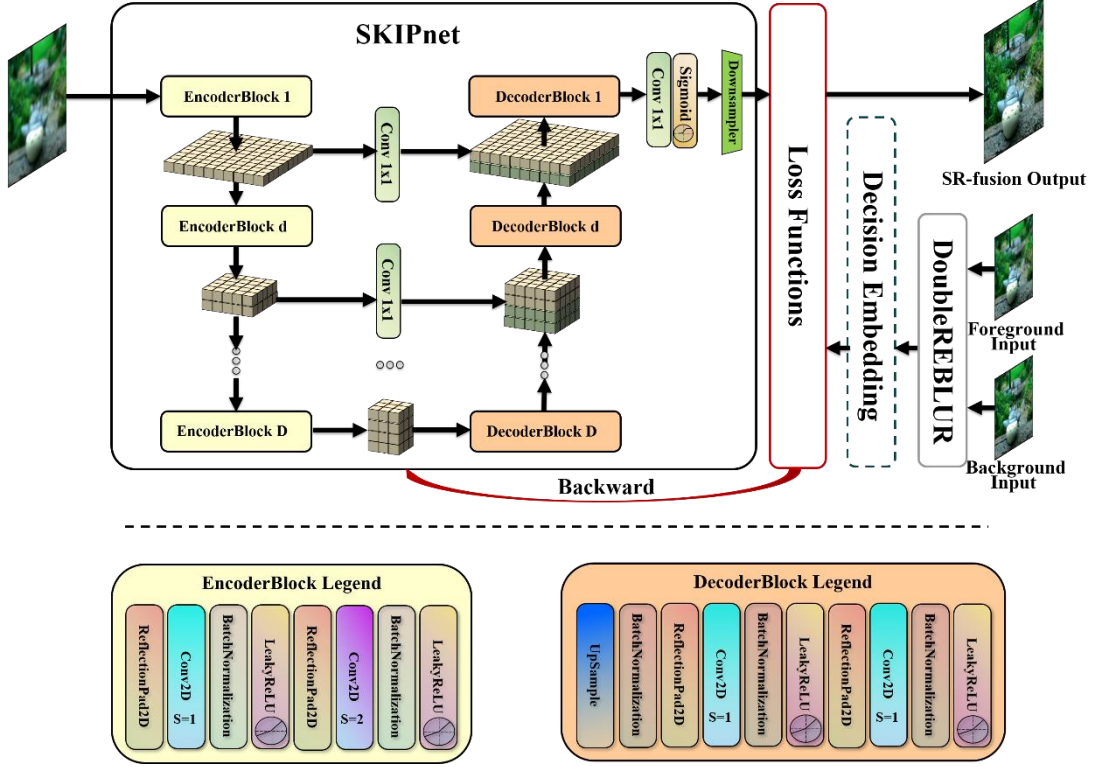


Fig. 2 DFP framework and SKIPnet architecture.

The details of SKIPnet architecture is illustrated in Fig. 1. Based on the encoder-decoder framework, the SKIPnet is divided into the encoder and decoder parts, and they are symmetric about the central feature map  $\phi_C$ . The backbone of the encoder part is composed of  $D$  encoder-blocks which extract feature maps for  $D$  scales. Each block consists of a reflection padding preparing layer, 1-strided  $n_d \times n_d$  convolution extracting layer, batch normalization processing layer, leaky-ReLU activating layer, reflection padding preparing layer, 2-strided  $n_d \times n_d$  convolution downsampling layer, batch normalization processing layer and leaky-ReLU activating layer, successively. Identically, the backbone of the decoder part is composed of  $D$  decoder-blocks which extract and fuse feature maps for  $D$  scales. Each block consists of a bilinear upsampling layer, batch normalization processing layer, reflection padding preparing layer, 1-strided  $n_d \times n_d$  convolution extracting layer, batch normalization processing layer, leaky-ReLU activating layer, reflection padding preparing layer, 1-strided  $n_d \times n_d$  convolution extracting layer, batch normalization processing layer and leaky-ReLU activating layer, successively. For multi-scale feature maps fusion, encoder part feature maps  $\phi_{v_d}^e(n)$  are concatenated to decoder part feature maps  $\phi_{u_d}^d(n)$ . In the end, a  $1 \times 1$  convolution is adopted to reduce dimensionality, and a sigmoid activation function is adopted to obtain the output format which demanded. In SKIPnet architecture, the downsampler with conventional approaches such as BILINEAR, BICUBIC and LANCZOS can be used to obtain the same size output to inputs, and the scale of the SR depends on the scale of the downsampler. Moreover, the depth  $D$  and the convolution kernel size  $n_d$  are adjustable parameters. For convenient parameter adjustment,  $D = 5$  and  $n_d = 5$  are used in DFP, two  $3 \times 3$  convolution layers can be used to replace the  $5 \times 5$  convolution layer for higher efficiency.

Although some CNN based methods including ResNets [53], DenseNets [54] and Residual Dense Network [46] have been proved to work better on extracting features than autocoder architecture, they often have poor performance in image prior extraction. However, the image prior relying on handcrafted network architecture such as encoder-decoder still works well.

### 3.2.2 DoubleReblur

As we known, most MFIF methods [4], [5], [6], [7], [8], [10], [15], [22], [23] are based on decision maps, which can be obtained by handcrafted focus measurement. Therefore, combining with computational imaging, morphological image processing and graphics, we propose the DoubleReblur focus measurement model as shown in Fig. 3.

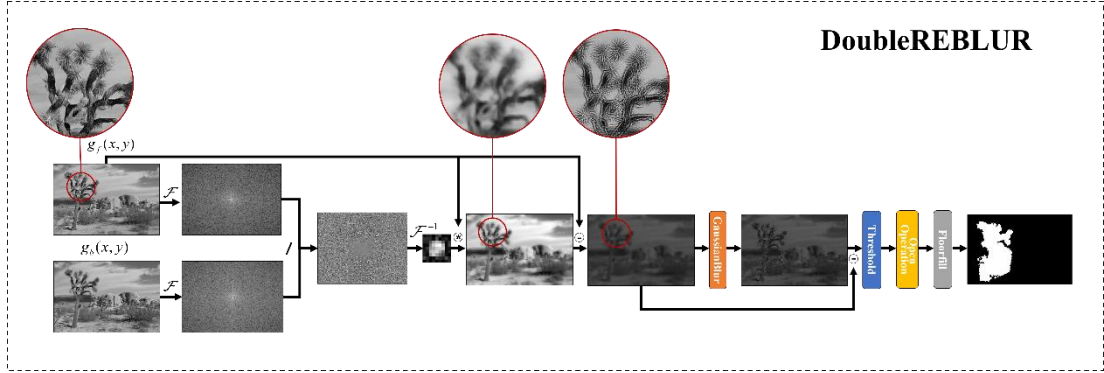


Fig. 3. Schematic illustration of DoubleReblur.

According to the imaging model in Eq. (1), the relation between the foreground input  $i_f(x,y)$  and the background input  $i_b(x,y)$  can be represented as Eq. (11).

$$i_b(x, y) = i_f(x, y) * h_s(x, y) + n_s(x, y) \quad (11)$$

To estimate the spread kernel  $h_s(x,y)$ , Fourier transform is implemented on both sides of Eq. (11) as follows:

$$\mathcal{F}\{i_b(x, y)\} = \mathcal{F}\{i_f(x, y) * h_s(x, y) + n_s(x, y)\} \quad (12a)$$

$$I_b(\xi, \eta) = I_f(\xi, \eta) \cdot H_s(\xi, \eta) + \mathcal{N}_s(\xi, \eta) \quad (12b)$$

where  $\mathcal{F}$  is the Fourier transform,  $I_b(\xi, \eta)$ ,  $I_f(\xi, \eta)$ ,  $H_s(\xi, \eta)$  and  $\mathcal{N}_s(\xi, \eta)$  are the frequency spectra of  $i_b(x,y)$ ,  $i_f(x,y)$ ,  $h_s(x,y)$  and  $n_s(x,y)$ , respectively.

$$\frac{I_b(\xi, \eta)}{I_f(\xi, \eta)} = \frac{I_f(\xi, \eta) \cdot H_s(\xi, \eta)}{I_f(\xi, \eta)} + \frac{\mathcal{N}_s(\xi, \eta)}{G_f(\xi, \eta)} \quad (13)$$

To remove the noise term, a low-pass filter  $\mathcal{T}$  is performed on Eq. (13). In the end, the estimate of spread kernel  $\hat{h}_s(x,y)$  can be obtained by follows:

$$\hat{h}_s(x, y) = \mathcal{F}^{-1} \left\{ \mathcal{T} \left[ \frac{I_f(\xi, \eta)}{I_b(\xi, \eta)} - \frac{\mathcal{N}_s(\xi, \eta)}{I_f(\xi, \eta)} \right] \right\} \quad (14)$$

The first reblur image can be obtained by Eq. (15).

$$\tilde{i}_b(x, y) = i_b(x, y) * \hat{h}_s(x, y) \quad (15)$$

Then, the Gaussian reblur  $\mathcal{G}$  is used to enhance the sharpness difference as  $s(x,y)$  obtained by Eq. (16).

$$s(x, y) = \left| \tilde{i}_b(x, y) - \mathcal{G}\{\tilde{i}_b(x, y)\} \right| \quad (16)$$

$d(x,y)$  can be obtained by performing threshold segmentation on sharpness difference image  $s(x,y)$ .

$$d(x, y) = \begin{cases} 1, & s(x, y) > t \\ 0, & s(x, y) \leq t \end{cases} \quad (17)$$

To eliminate gaps and holes, dilating and eroding are defined as closed operation •



$$\hat{d}(x, y) = d(x, y) \bullet E \quad (18)$$

The decision map  $m(x, y)$  can be finally obtained using the largest region floorfill algorithm  $\mathcal{C}$ .

$$m(x, y) = \mathcal{C} \left\{ \hat{d}(x, y) \right\} \quad (19)$$

There are 5 parameters in DoubleReblur as  $[k_g, k_d, k_e, t, f]$ :  $k_g$  is the kernel size of Gaussian blur,  $k_d$  is the kernel size of dilating,  $k_e$  is the kernel size of eroding,  $t$  is the threshold of segmentation, and  $f$  is the bool flag controlling if the largest region filling is used. We transform the image to Y channel and use [5, 3, 3, 0.01, 1] for most images and slightly adjust parameters for different image details.

### 3.2.3 Decision Embedding

Since the decision maps are obtained from handcrafted focus measurement, they suffer from disadvantages such as edge fragmentation and false determination. In order to optimize the handcrafted decision maps, learning-based decision embedding is designed as Fig. 4. The input is obtained by the average of low-resolution inputs and can also be replaced by random noise, and the binarized decision map can be generated by SKIPnet. Moreover, we design a optimized loss function  $\mathcal{L}_{opt}$  as Eq. (20) to optimize the decision via minimizing the difference between focus measurement regions and original low-resolution inputs.

$$\mathcal{L}_{opt} = \frac{1}{H \cdot W} \sum_i \sum_j \left| \hat{m}_{i,j} - m_{i,j} \right| + \left| \hat{m}_{i,j} \cdot I_{fore_{i,j}} - I_{fore_{i,j}} \right| + \left| (1 - \hat{m}_{i,j}) \cdot I_{back_{i,j}} - I_{back_{i,j}} \right| \quad (20)$$

where  $H$  and  $W$  are the height and width of the image,  $I_{fore}$  and  $I_{back}$  are the foreground and background low-resolution inputs,  $m$  is the handcrafted decision map obtained by DoubleReblur,  $\hat{m}$  is the optimized decision map generated by SKIPnet. Algorithm 2 briefly demonstrates the decision embedding process.

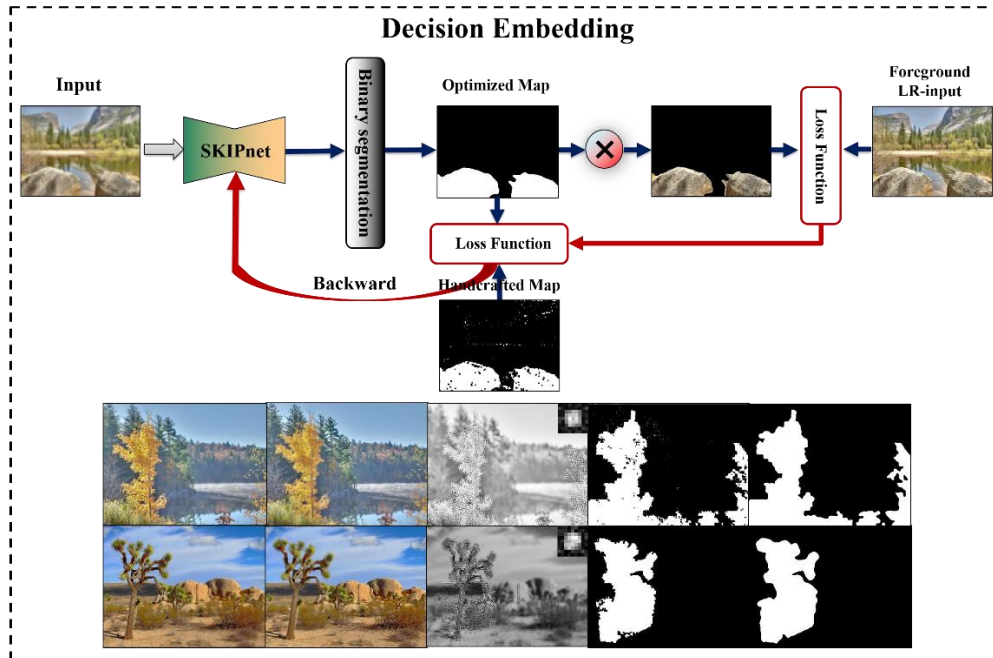


Fig. 4. Schematic illustration of decision embedding and some examples.

---

**Algorithm 2** Decision Embedding

---

```
1:   Input: foreground input  $I_{fore}$ , background input  $I_{back}$ , input  $n$  and handcrafted decision map  $m$ 
      which obtained by DoubleREBLUR;
2:   for iterations  $K=500$  do
3:     Forward:  $\hat{m} = \text{SKIPnet}(\text{input } n)$ ;
4:     for  $x, y$  in  $\hat{m}$  do
5:       if  $\hat{m}(x,y) > 0.5$ ,  $\hat{m}(x,y)=1$ ;
6:       else  $\hat{m}(x,y)=0$ ;
7:     end for
8:      $\mathcal{L}_{opt} = \frac{1}{H \cdot W} \sum_i \sum_j |\hat{m}_{i,j} - m_{i,j}| + |\hat{m}_{i,j} \cdot I_{fore_{i,j}} - I_{fore_{i,j}}| + |(1 - \hat{m}_{i,j}) \cdot I_{back_{i,j}} - I_{back_{i,j}}|$ 
9:     Backward to update SKIPnet parameters  $\Theta$ ;
10:  end for
11:  Output:  $\hat{m}, 1-\hat{m}$  ;
```

---

### 3.2.4 Loss Functions

The designed loss functions as Eq. (21) are composed of content loss  $\mathcal{L}_{con}$ , joint gradient loss  $\mathcal{L}_{j\_grad}$  and gradient limit loss  $\mathcal{L}_{grad}$ :

the content loss is to constrain the SKIPnet to learn the clear region of each image, the joint gradient loss is to enhance the SKIPnet to learn the high-frequency information and to reduce the dependency on decision maps, and the gradient limit loss is to reduce the noise and oscillation effects.  $\alpha$ ,  $\beta$  and  $\gamma$  in Eq. (21) are weighted parameters, and set as 1, 0.5 and 0.1.

$$\mathcal{L} = \alpha \mathcal{L}_{con} + \beta \mathcal{L}_{j\_grad} + \gamma \mathcal{L}_{grad} \quad (21)$$

$$\mathcal{L}_{con} = \frac{1}{H \cdot W} \sum_i \sum_j \lambda_1 \hat{m} \cdot \left| \hat{I}_{MFISRF_{i,j}} - I_{fore_{i,j}} \right| + \lambda_2 (1 - \hat{m}) \cdot \left| \hat{I}_{MFISRF_{i,j}} - I_{back_{i,j}} \right| \quad (22)$$

$\mathcal{L}_{con}$  in Eq. (22) is the content loss, where  $\lambda_1$  and  $\lambda_2$  are weighted parameters both equal to 1. For generated MFISRF image  $\hat{I}_{MFISRF}$ , the sharpness information is desired, therefore, the focus regions in  $I_{fore}$  and  $I_{back}$  are obtained via doting decision maps.  $L_1$  norms between the foreground focus region of  $\hat{I}_{MFISRF}$  and  $I_{fore}$ , and between the background focus region of  $\hat{I}_{MFISRF}$  and  $I_{back}$  are used to compute their distances. Rather than  $L_1$  norm,  $L_2$  norm has stronger penalty for large errors and weaker penalty for small errors, and ignores the effect of the image content itself. It is worth noting the human visual system (HVS) is especially sensitive to brightness and color changes in untextured areas of the image, and [68] has proved that  $L_1$  norm performs better than  $L_2$  norm in SR tasks, so  $L_1$  norm is adopted here.

$$\mathcal{L}_{j\_grad} = \frac{1}{H \cdot W} \sum_i \sum_j \left| \nabla_L \hat{I}_{MFISRF_{i,j}} - \max(\nabla_L I_{fore_{i,j}}, \nabla_L I_{back_{i,j}}) \right| \quad (23)$$

$\mathcal{L}_{j\_grad}$  in Eq. (23) is the joint gradient loss, where  $\nabla_L$  is the gradient obtained via Laplacian. The difference between focus and defocus regions are almost the high-frequency information, and moreover, the Laplacian gradient map can well describe high-frequency information. For MFIF, the maximal Laplacian gradient map of unfused inputs almost equals to the fused image. For SR, the Laplacian gradient map can provide more high-frequency details. Therefore,  $L_1$  norm between the Laplacian gradient map of generated MFISRF image  $\hat{I}_{MFISRF}$  and the joint maximal Laplacian gradient map of low-resolution inputs  $I_{fore}$  and  $I_{back}$  is used to compute their distance.

$$\mathcal{L}_{grad} = \frac{1}{H \cdot W} \sum_i \sum_j (\nabla_x \hat{I}_{MFISRF_{i,j}} + \nabla_y \hat{I}_{MFISRF_{i,j}}) \quad (24)$$

$\mathcal{L}_{grad}$  in Eq. (24) is the gradient limit loss. Unfortunately, DFP exploits the self-similarity property of input images themselves for reconstruction, it will cause some noise and oscillation. Therefore, the gradient limit loss is used to reduce these noise and oscillation effects.

## 4 EXPERIMENTAL RESULTS

### 4.1 Qualitative Experimental Results

First, we qualitatively compare our DFP with the combinations of learning-based MFIF (CNN[22], DRPL[23], ECNN[24], IFCNN[25], MADCNN[26], PCANet[27], FusionDN[28], GCF[29], SESF[30], MFF-GAN[1], PMGI[31], U2Fusion[32]) and conventional SR (Bicubic), the combinations of learning-based MFIF (CNN, DRPL, ECNN, IFCNN, MADCNN, PCANet, FusionDN, GCF, SESF, MFF-GAN, PMGI, U2Fusion) and unsupervised SR (DIP[64]) and the combinations of learning-based MFIF (CNN, DRPL, ECNN, IFCNN, MADCNN, PCANet, FusionDN, GCF, SESF, MFF-GAN, PMGI, U2Fusion) and supervised SR (SRCNN[41]). Methods relying on combinations of MFIF and SR work with two models and learn from large datasets, while DFP works with only one model and learns without any dataset.



Fig. 5 Qualitative ×2 MFISRF comparison of our U2Fusion on MFI-WHU 15.



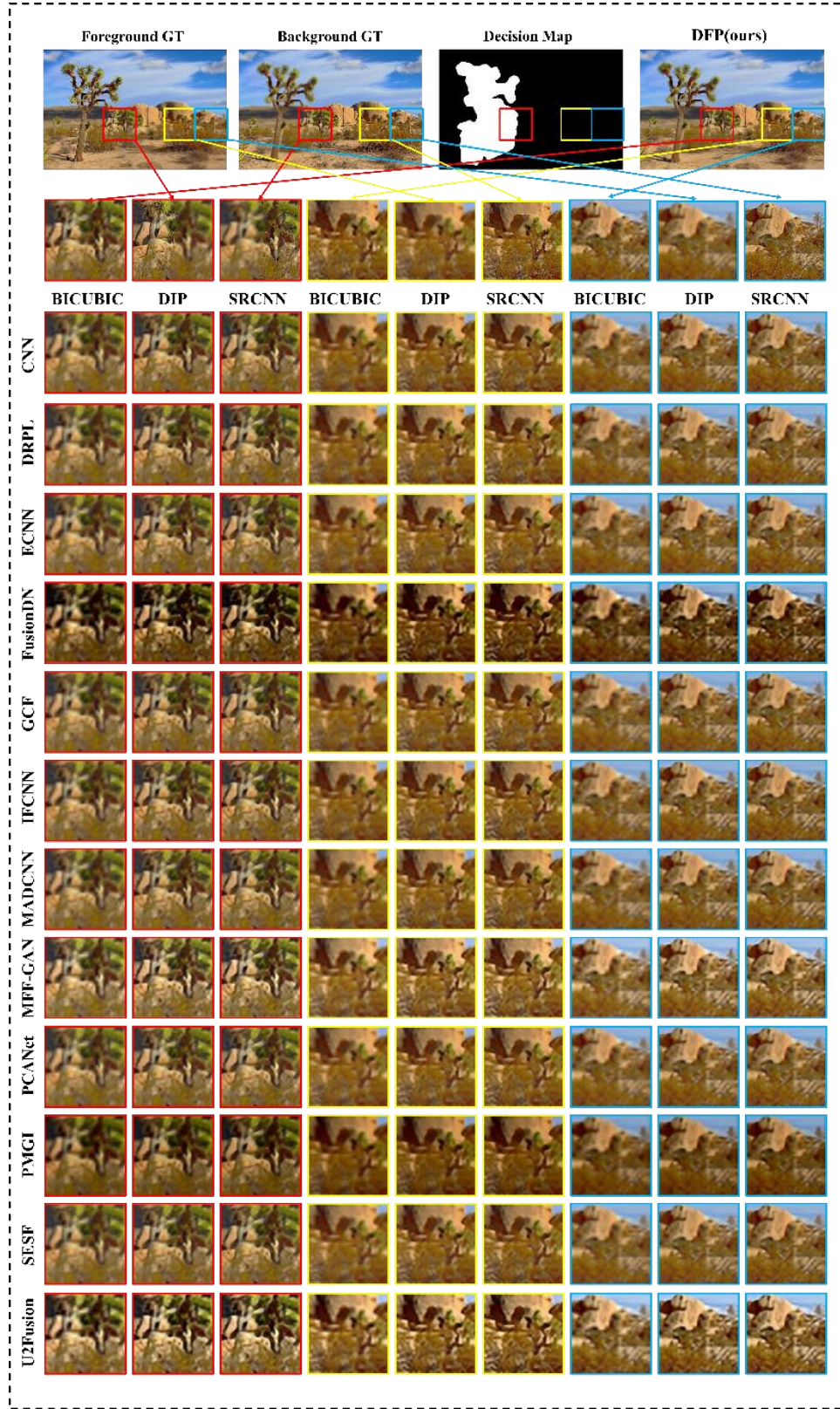


Fig. 6. Qualitative  $\times 4$  MFISRF comparison of our U2Fusion on MFI-WHU 01.

Figs. 5 and 6 are the visual results of MFISRF  $\times 2$  and  $\times 4$  on MFI-WHU 15 and MFI-WHU 01. In MFIF, CNN, DRPL, ECNN, IFCNN, MADCNN, PCANet and GCF provide similar results with almost discernible difference, but they all suffer from poor MFIF quality. PMGI improves the MFIF performance; however, it is compatible with multi-task such as infrared and visible image fusion, multi-exposure image fusion and medical image fusion, and these tasks are of in low contrast cases, so the PMGI results are often dark, blurred and edge enhanced. While SESF slightly improves the MFIF performance compared to PMGI by increasing the brightness and reducing the blur. FusionDN and its upgraded U2Fusion also compatible with the multi-task have better MFIF performance than above methods; however, they still could not completely solve problems such as dark, blur and enhanced edge in MFIF. In SR, DIP improves image quality to some

extent, but since only self-similarity and low-level statistical priors are used, high frequency details are lost especially in defocus and vista regions. Although SRCNN performs better than DIP, it relies on training with large datasets which composed of fixed low- and high-resolution image pairs. Generally, it is easy to note that the unsupervised methods (FusionDN, GCF, SESF, MFF-GAN, PMGI) performed better than the supervised methods (CNN, DRPL, ECNN, IFCNN, MADCNN, PCANet) in MFIF; but contrarily, the supervised method (SRCNN) performed better than the unsupervised methods (Bicubic, DIP) in SR. Even DFP does not use any datasets for training, it still achieves high-quality results comparable to those obtained via the combinations of the unsupervised MFIF (FusionDN, GCF, SESF, MFF-GAN, PMGI, U2Fusion) and the supervised SR (SRCNN), proving the high performance of MFISRF when using our proposed method.

#### 4.2 Quatitative Experimental Results

Besides qualitative comparisons, quantitative comparisons are performed still using the MFI-WHU benchmark evaluation dataset [1]. The evaluation metrics include mean gradient (MG), edge intensity (EI), information entropy (IE), mean gray value (MGA), and polar edge coherence (ECO) [69], respectively. MG reflects the rate of contrast change of tiny details in the image explained in Eq. (24a), in which  $H$  and  $W$  are image height and width,  $\nabla_x$  and  $\nabla_y$  present gradient in x- and y-directions, and  $I$  is the image. RMG represents the relative MG between ground truth and MFISRF as demonstrated in Eq. (24b).

$$MG = \frac{1}{H \cdot W} \sum_i \sum_j (\nabla_x I_{i,j} + \nabla_y I_{i,j}) \quad (24a)$$

$$RMG = \left| MG_{MFISRF} - \frac{MG_{GT}^1 + MG_{GT}^2}{2} \right| \quad (24b)$$

The most basic feature of an image is its edge which exists between target and background, so it is one of the most important features to evaluate image fusion. EI is a quantitative coefficient to describe edge information explained by Eq. (25a), in which  $h_x$  and  $h_y$  are Sobel operators in x- and y-directions, and  $*$  represents convolution. RMG represents the relative EI between ground truth and MFISRF as demonstrated in Eq. (25b).

$$EI = \frac{1}{H \cdot W} \sqrt{\sum_i \sum_j [(I * s_x)^2 + (I * s_y)^2]} \quad (25a)$$

$$REI = \left| EI_{MFISRF} - \frac{EI_{GT}^1 + EI_{GT}^2}{2} \right| \quad (25b)$$

IE reflects the comprehensive characteristics of gray value at a pixel position and its surrounding pixel gray distribution, and is demonstrated by Eq. (26a), where  $f(i, j)$  is the frequency of occurrence of characteristic binary group  $(I_i, I_j)$ . RIE represents the relative IE between ground truth and MFISRF as demonstrated in Eq. (26b).

$$IE = - \sum_i \sum_j \frac{f(i, j)}{H \cdot W} \lg \frac{f(i, j)}{H \cdot W} \quad (26a)$$

$$RIE = \left| IE_{MFISRF} - \frac{IE_{GT}^1 + IE_{GT}^2}{2} \right| \quad (26b)$$

MGA shown in Eq. (27a) is the average level of image gray, which represents the overall brightness level of the image. RIE represents the relative MGA between ground truth and MFISRF as demonstrated in Eq. (27b).

$$MGA = \frac{1}{H \cdot W} \sum_i \sum_j I_{i,j} \quad (27a)$$

$$RMGA = \left| MGA_{MFISRF} - \frac{MGA_{GT}^1 + MGA_{GT}^2}{2} \right| \quad (27b)$$

RECO reflects the edge similarity of the reconstructed image and the original image illustrated in Eq. (28a), where ECO is edge coherence according to [69], GTs are the ground truth of inputs, SRF is the output image, C is a regularization constant. RECO represents the relative ECO between ground truth and MFISRF as demonstrated in Eq. (28b).

$$RECO = \left| 2 - \frac{ECO_{MFISRF} + C}{ECO_{GT}^{fore} + C} - \frac{ECO_{MFISRF} + C}{ECO_{GT}^{back} + C} \right| \quad (28)$$

We compare our DFP with the combinations of 12 fusion methods and 3 SR methods. 12 fusion including 6 supervised learning methods: CNN, DRPL, ECNN, IFCNN, MADCNN, PCANet and 6 unsupervised learning methods: FusionDN, GCF, SESF, MFF-GAN, PMGI, U2Fusion. 3 SR methods including conventional method BICUBIC, unsupervised learning method DIP, supervised learning method SRCNN. All methods except DIP are trained based on large datasets. However, DFP works without dataset.

TABLE 1. Quatitative comparison of our U2Fusion and combinations of MFIF and interpolated SR on MFI-WHU

METHOD	CATEGORY	RMG	REI	RIE	RMGA	RECO
		×2 ×4	×2 ×4	×2 ×4	×2 ×4	×2 ×4
CNN	SUPERVISED	0.7207	3.6682	0.0176	0.1692	0.0844
BICUBIC	/	2.5906	22.7946	0.0598	0.1723	0.0488
DRPL	SUPERVISED	0.6510	<b>3.0538</b>	0.0160	<b>0.0883</b>	0.0895
BICUBIC	/	2.5675	22.5395	0.0573	<b>0.0957</b>	0.0458
ECNN	SUPERVISED	0.6724	3.2677	0.0171	<b>0.1049</b>	0.0725
BICUBIC	/	2.5747	22.6202	0.0580	<b>0.1032</b>	0.0363
IFCNN	SUPERVISED	<b>0.4649</b>	<b>1.8060</b>	<b>0.0151</b>	0.5009	0.0261
BICUBIC	/	2.4400	21.1481	<b>0.0535</b>	0.4719	<b>0.0102</b>
MADCNN	SUPERVISED	0.6525	<b>3.0449</b>	<b>0.0158</b>	<b>0.1290</b>	0.1046
BICUBIC	/	2.5562	22.4198	<b>0.0572</b>	0.1299	0.0602
PCANet	SUPERVISED	0.7444	3.8778	0.0174	0.2240	<b>0.0196</b>
BICUBIC	/	2.6040	22.9440	0.0612	0.2252	0.0283
FusionDN	UNSUPERVISED	0.9637	12.3182	0.3491	16.4175	0.0014
BICUBIC	/	<b>1.7848</b>	<b>14.4899</b>	0.3231	16.3919	<b>0.0281</b>
GCF	UNSUPERVISED	0.6742	3.2527	0.0173	0.1370	0.1026
BICUBIC	/	2.5759	22.6316	0.0594	<b>0.1271</b>	0.0639
SESF	UNSUPERVISED	0.7138	3.5747	<b>0.0159</b>	0.1735	<b>0.0214</b>
BICUBIC	/	2.5856	22.7406	0.0591	0.1686	0.0290
MFF-GAN	UNSUPERVISED	<b>0.5588</b>	9.0613	0.1219	3.3443	0.0477
BICUBIC	/	2.0095	16.3748	0.0827	3.3727	0.0506
PMGI	UNSUPERVISED	2.1311	18.4735	0.3899	18.1909	0.1422
BICUBIC	/	2.9701	27.0107	0.3921	18.1691	0.1434
U2Fusion	UNSUPERVISED	0.9618	15.1490	0.2975	5.3168	0.0955
BICUBIC	/	<b>1.3636</b>	<b>9.3573</b>	0.2461	5.3213	0.1481
DFP(ours)	UNSUPERVISED	<b>0.5840</b>	6.3614	0.0222	0.5324	<b>0.0056</b>
	DATASET-FREE	<b>1.8111</b>	<b>14.8770</b>	<b>0.0376</b>	0.5536	<b>0.0062</b>

TABLE 2. Quatitative comparison of our U2Fusion and combinations of MFIF and unsupervised SR on MFI-WHU

METHOD	CATEGORY	RMG	REI	RIE	RMGA	RECO
		×2 ×4	×2 ×4	×2 ×4	×2 ×4	×2 ×4
CNN	SUPERVISED	0.5780	2.6387	0.0310	<b>0.3439</b>	0.0863
DIP	UNSUPERVISED	2.0613	17.1756	0.0509	<b>0.3378</b>	0.0652
DRPL	SUPERVISED	<b>0.5019</b>	<b>2.4955</b>	0.0297	0.4475	0.0884
DIP	UNSUPERVISED	2.0509	17.0586	0.0485	0.4205	0.0608
ECNN	SUPERVISED	0.5301	<b>2.3584</b>	0.0310	0.4366	0.0690
DIP	UNSUPERVISED	2.0475	17.0193	0.0503	0.4090	0.0512
IFCNN	SUPERVISED	<b>0.3421</b>	2.9407	<b>0.0227</b>	0.9985	0.0343
DIP	UNSUPERVISED	1.8643	15.0243	<b>0.0447</b>	0.3769	<b>0.0064</b>
MADCNN	SUPERVISED	<b>0.4957</b>	<b>2.2916</b>	0.0310	0.4080	0.1036
DIP	UNSUPERVISED	2.0539	17.0954	<b>0.0460</b>	0.3769	0.0817
PCANet	SUPERVISED	0.6014	2.7950	0.0288	<b>0.2661</b>	<b>0.0192</b>
DIP	UNSUPERVISED	2.0911	17.5025	0.0559	<b>0.2713</b>	<b>0.0233</b>
FusionDN	UNSUPERVISED	1.1171	14.3756	0.3529	16.7732	<b>0.0158</b>
DIP	UNSUPERVISED	<b>1.2079</b>	<b>9.5311</b>	0.3429	16.7444	0.0317
GCF	UNSUPERVISED	0.5141	2.5166	0.0276	0.4342	0.1009
DIP	UNSUPERVISED	2.0636	17.1856	0.0539	0.4224	0.0824
SESF	UNSUPERVISED	0.5593	2.6525	<b>0.0275</b>	<b>0.3503</b>	0.0244
DIP	UNSUPERVISED	2.0534	17.0854	0.0474	<b>0.3486</b>	0.0245
MFF-GAN	UNSUPERVISED	0.8850	12.7859	0.1358	3.1079	0.0585
DIP	UNSUPERVISED	1.8308	<b>8.2245</b>	0.1041	3.1314	0.0377
PMGI	UNSUPERVISED	2.2334	19.5217	0.4057	18.5801	0.1329
DIP	UNSUPERVISED	2.6718	24.0968	0.4118	18.5721	0.1468
U2Fusion	UNSUPERVISED	1.1756	17.2388	0.2929	5.2692	0.0940
DIP	UNSUPERVISED	<b>0.5697</b>	<b>3.9655</b>	0.2739	5.3012	0.1389
DFP(ours)	UNSUPERVISED	0.5840	6.3614	<b>0.0222</b>	0.5324	<b>0.0056</b>
	DATASET-FREE	<b>1.8111</b>	<b>14.8770</b>	<b>0.0376</b>	0.5536	<b>0.0062</b>

TABLE 3. Quatitative comparison of our U2Fusion and combinations of MFIF and supervised SR on MFI-WHU

METHOD	CATEGORY	RMG	REI	RIE	RMGA	RECO
		$\times 2$ $\times 4$	$\times 2$ $\times 4$	$\times 2$ $\times 4$	$\times 2$ $\times 4$	$\times 2$ $\times 4$
CNN	SUPERVISED	<b>0.7995</b>	9.9926	<b>0.0237</b>	0.9516	0.0827
SRCNN	SUPERVISED	1.7145	13.6249	0.0317	<b>0.7879</b>	0.0705
DRPL	SUPERVISED	0.9117	11.0625	0.0261	1.0490	0.0883
SRCNN	SUPERVISED	1.6749	13.1979	<b>0.0290</b>	0.8682	0.0695
ECNN	SUPERVISED	0.8786	10.7192	0.0259	1.0448	0.0692
SRCNN	SUPERVISED	1.6891	13.3493	0.0303	0.8679	0.0598
IFCNN	SUPERVISED	1.0715	13.0042	0.0355	1.5993	0.0378
SRCNN	SUPERVISED	1.4554	10.8233	<b>0.0240</b>	1.4270	<b>0.0092</b>
MADCNN	SUPERVISED	0.8807	10.8249	0.0265	1.0127	0.1025
SRCNN	SUPERVISED	1.6566	13.0050	<b>0.0283</b>	0.8423	0.0834
PCANet	SUPERVISED	<b>0.7987</b>	<b>9.7746</b>	<b>0.0235</b>	<b>0.8760</b>	<b>0.0133</b>
SRCNN	SUPERVISED	1.7302	13.7981	0.0341	<b>0.7250</b>	<b>0.0082</b>
FusionDN	UNSUPERVISED	1.8200	22.2081	0.3592	17.1748	<b>0.0138</b>
SRCNN	SUPERVISED	<b>0.9588</b>	<b>8.5307</b>	0.3476	17.0702	0.0312
GCF	UNSUPERVISED	0.8737	<b>0.0241</b>	10.6861	<b>0.0241</b>	0.0968
SRCNN	SUPERVISED	1.6905	13.3631	0.0311	0.8797	0.0864
SESF	UNSUPERVISED	0.8097	10.1118	0.0249	0.9539	0.0153
SRCNN	SUPERVISED	1.7054	13.5246	0.0316	0.7985	0.0095
MFF-GAN	UNSUPERVISED	2.2016	24.7978	0.1562	2.9512	0.0651
SRCNN	SUPERVISED	<b>0.8676</b>	<b>5.2269</b>	0.1060	2.9792	0.0338
PMGI	UNSUPERVISED	1.7301	15.1158	0.3925	19.0188	0.1293
SRCNN	SUPERVISED	2.4111	21.4495	0.3913	18.9211	0.1447
U2Fusion	UNSUPERVISED	2.1945	26.6641	0.3184	5.3172	0.0778
SRCNN	SUPERVISED	<b>0.4994</b>	<b>6.2283</b>	0.2815	5.3075	0.1156
DFP(ours)	UNSUPERVISED	<b>0.5840</b>	<b>6.3614</b>	<b>0.0222</b>	<b>0.5324</b>	<b>0.0056</b>
	DATASET-FREE	1.8111	14.8770	0.0376	<b>0.5536</b>	<b>0.0062</b>

Tables 1-3 quantitatively compare the MFIF and SR performance of combining methods and the proposed MFISRF one using above evaluation coefficients. Red, green and blue colors mark the 1st, 2nd and 3rd best of the performance. According to these tables, our proposed MFISRF often can achieve high-quality super resolved multi-focus fused image in both  $\times 2$  and  $\times 4$  conditions. Especially, even compared to the optimized combinations of unsupervised MFIF methods and supervised SR method, our proposed DFP could still obtain rather low RMG, REI, RIE, RMGA and RECO values even lower or very close to the those obtained by those optimized MFIF and SR method combinations.

## 5 DISCUSSION

Still, many methods perform well in MFISRF such as FusionDN, MFF-GAN, PMGI and U2Fusion. Significantly, the difference between implementing MFISRF and MFIF with DFP is only downsampling, so the equivalent comparison should be DFP and the combination of unsupervised MFIF and interpolation SR. Therefore, the additional  $\times 2$  MFISRF results on MFI-WHU 03[1], MFI-WHU 11[1], Lytro 11[67] and Lytro 14[67] obtained by DFP and the combinations of PMGI, FusionDN, U2Fusion, MFF-GAN and bicubic interpolation are listed in Fig. 7. It is observed that our DFP results are very similar to ground truth (GT) in both brightness, contrast, edge and color, and also much better than other competitors in both MFIF and SR quality. Especially, the results of FusionDN, MFF-GAN, PMGI and U2Fusion are excessively edge enhanced, and the reason is that these methods are constructed with models and loss functions highly relied on gradients which significantly improving image sharpness and visual perception but deviating from the ground truth. While DFP combines focus measurement and image prior to form an unsupervised closed-loop and utilizes the weighted joint gradient loss to reduce the dependency of focus measurement, therefore its results well balance the edge enhancement and image authenticity.



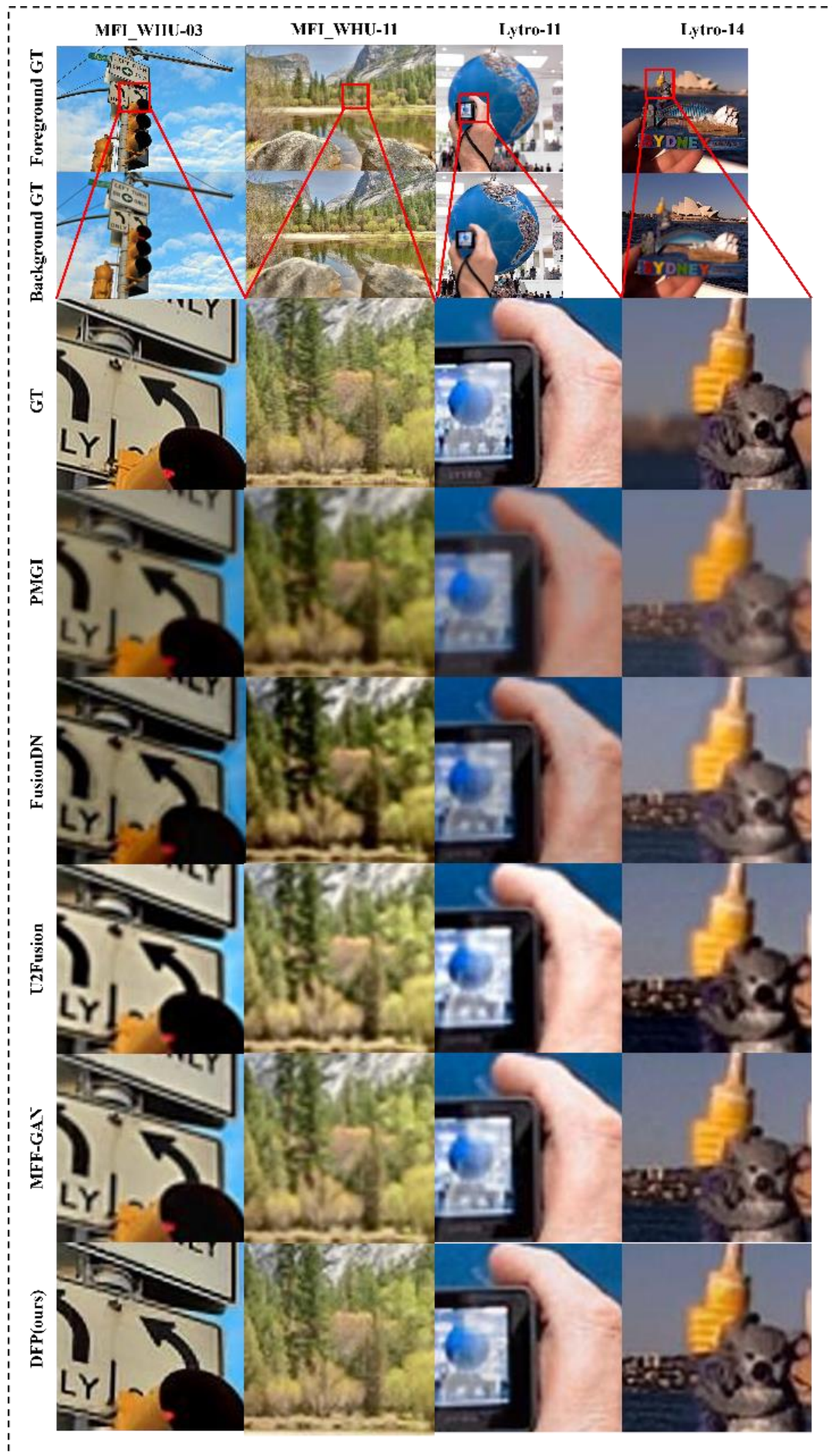


Fig. 7. Comparison of our U2Fusion and combinations of unsupervised MFIF and bicubic SR on  $\times 2$  MFISRF



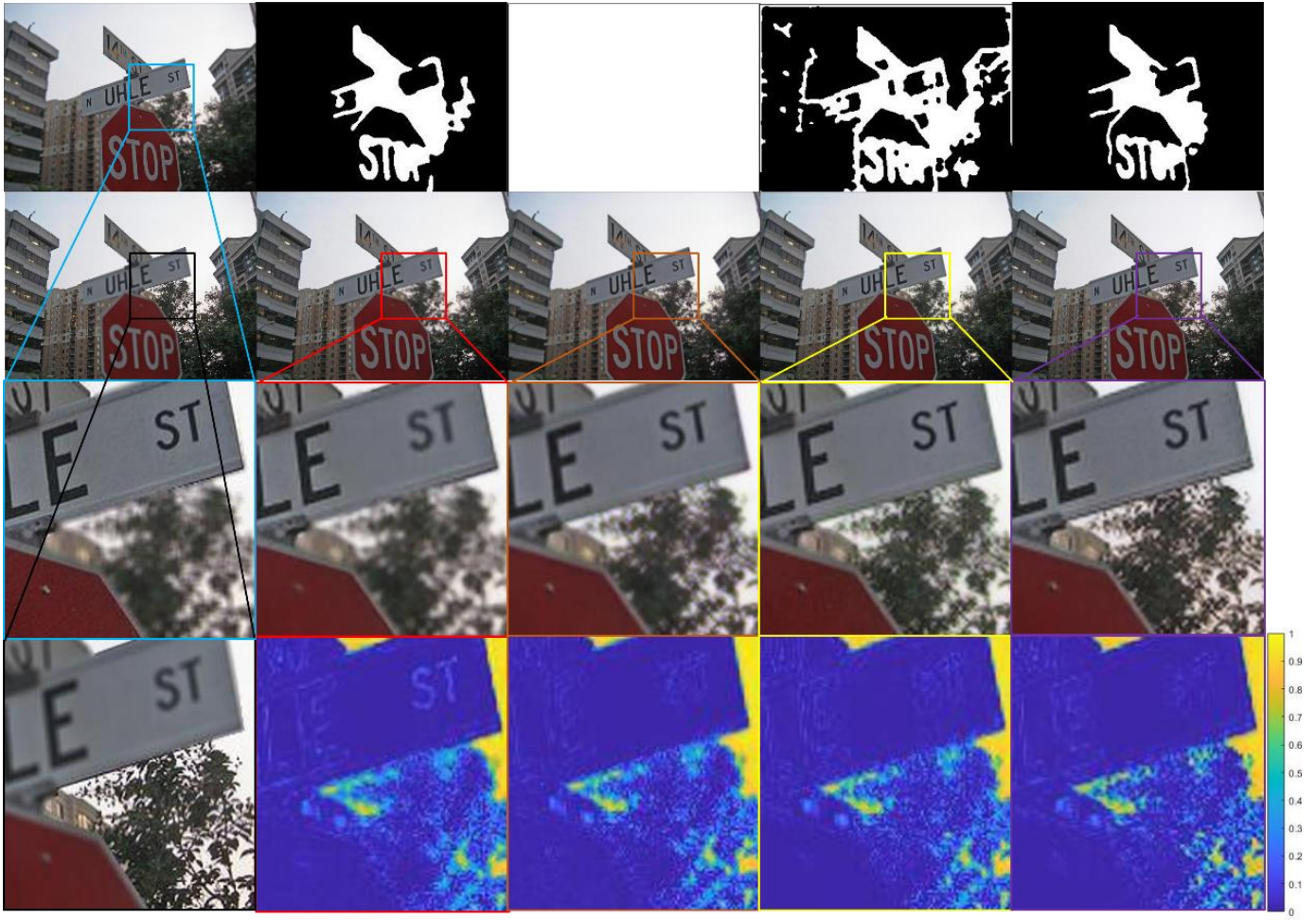


Fig. 8. Robustness comparison of our U2Fusion on  $\times 2$  MFISRF

Fig.8. lists the results on MFI-WHU 29 to prove the DFP robustness. The first column images are the foreground and background ground truths. The second column results are obtained by DFP with the DoubleReblur parameter set as  $[3,5,5,0.05,1]$  and without weighted joint gradient loss: the first image is the foreground decision map, the second image is the MFISRF image, the third one is the zoomed-in field-of-interest, and the last one is the pseudo-color image depicting the difference of ground truth and MFISRF result in Y channel. Identically, the images in the third, fourth and fifth columns are obtained by DFP but with different DoubleReblur parameter sets as  $[3,5,5,0,1]$ ,  $[3,5,5,0.01,1]$  and  $[3,5,5,0.05,1]$ , respectively. According to these results, it is proved that DFP has strong robustness since it can always provide high-quality MFIF results no matter the decision maps are good or bad; however, high-quality SR performance still depends on correct decision maps. Moreover, Fig. 9. reveals the training details of DFP and DIP still on the same MFI-WHU 29 with 3000 iterations. As DFP is multi-image SR while DIP is single-image SR, PSNR is less concerned here, while the convergence is more focused. According to the results, DFP converges only using  $\sim 400$  iterations, however, DIP does not converge until  $\sim 2500$  iterations. Additionally, DFP has a smoother trend with less fluctuations than DIP. Both results in Figs. 11 and 12 demonstrate the proposed DFP is robust in the MFISRF task.

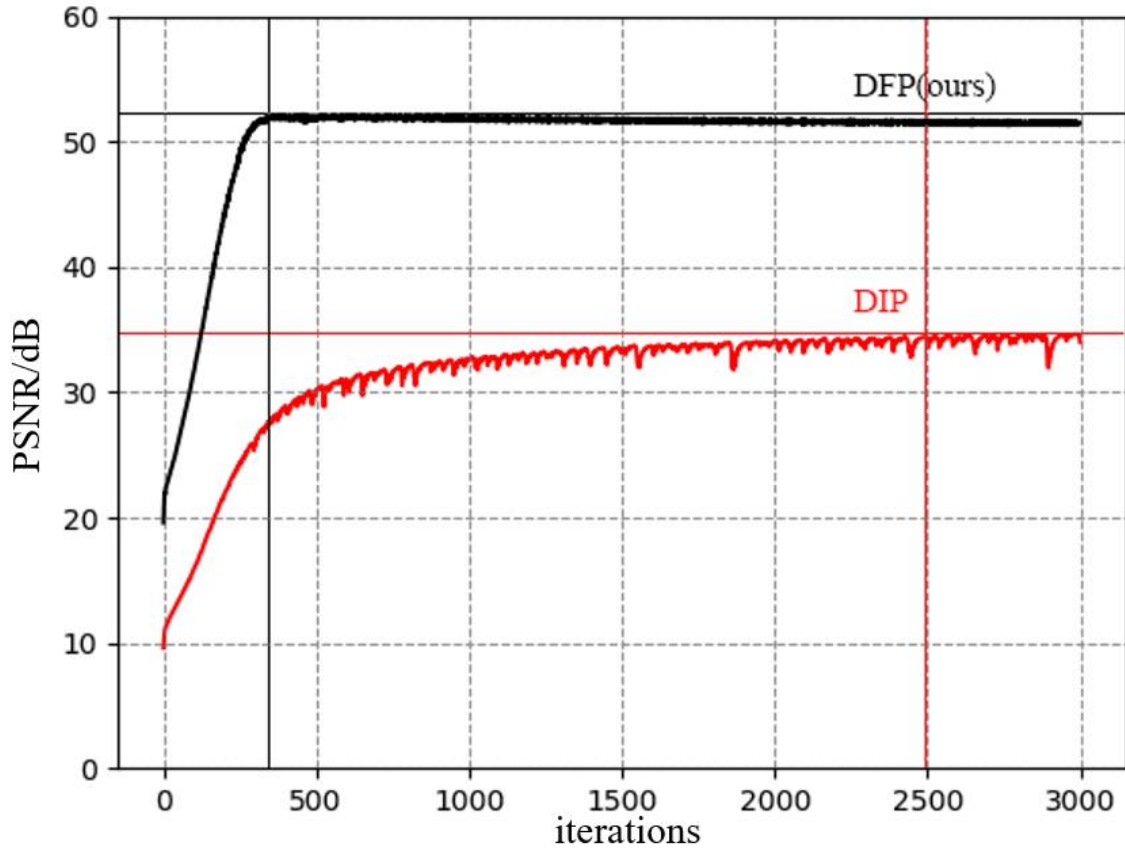


Fig. 9. Robustness comparison of our U2Fusion and DIP.

## 7 CONCLUSION

In this study, we unify the MFIF and blind SR problems as the MFISRF task, and propose a new unified dataset-free unsupervised framework DFP to address such MFISRF task. DFP consists of our designed SKIPnet end-to-end generated network to implement unsupervised learning via deep image prior, DoubleReblur tactic for focus measurement based on estimated PSF and Gaussian kernels convolution, decision embedding learned module for decision map optimization, and loss functions to guarantee high-quality MFISRF results robustly. Compared to 12 MFIF and 3 SR method combinations including both supervised and unsupervised ones, the proposed unsupervised dataset-free DFP approaches and even outperforms these state-of-art MFIF and SR method combinations. Furthermore, DFP is a general framework, thus its networks and focus measurement tactics can be continuously updated to further improve the MFISRF performance. We believe DFP can be potentially used in various computational photography applications.

## REFERENCES

- [1] H. Zhang, Z. Le, Z. Shao, H. Xu, and J. Ma, “MFF-GAN: An unsupervised generative adversarial network with adaptive and gradient joint constraints for multi-focus image fusion,” *Inf. Fusion*, vol. 66, no. September 2020, pp. 40–53, 2021, doi: 10.1016/j.inffus.2020.08.022.
- [2] J. Tian, L. Chen, L. Ma, and W. Yu, “Multi-focus image fusion using a bilateral gradient-based sharpness criterion,” *Opt. Commun.*, vol. 284, no. 1, pp. 80–87, 2011, doi: 10.1016/j.optcom.2010.08.085.
- [3] B. K. Shreyamsha Kumar, “Image fusion based on pixel significance using cross bilateral filter,” *Signal, Image Video Process.*, vol. 9, no. 5, pp. 1193–1204, 2015, doi: 10.1007/s11760-013-0556-9.
- [4] Y. Liu, S. Liu, and Z. Wang, “Multi-focus image fusion with dense SIFT,” *Inf. Fusion*, vol. 23, pp. 139–155, 2015, doi: 10.1016/j.inffus.2014.05.004.

- [5] X. Qiu, M. Li, L. Zhang, and X. Yuan, "Guided filter-based multi-focus image fusion through focus region detection," *Signal Process. Image Commun.*, vol. 72, no. December 2018, pp. 35–46, 2019, doi: 10.1016/j.image.2018.12.004.
- [6] S. Li, X. Kang, J. Hu, and B. Yang, "Image matting for fusion of multi-focus images in dynamic scenes," *Inf. Fusion*, vol. 14, no. 2, pp. 147–162, 2013, doi: 10.1016/j.inffus.2011.07.001.
- [7] J. Ma, Z. Zhou, B. Wang, and M. Dong, "Multi-focus image fusion based on multi-scale focus measures and generalized random walk," *Chinese Control Conf. CCC*, no. 1, pp. 5464–5468, 2017, doi: 10.23919/ChiCC.2017.8028223.
- [8] J. Ma, Z. Zhou, B. Wang, L. Miao, and H. Zong, "Multi-focus image fusion using boosted random walks-based algorithm with two-scale focus maps," *Neurocomputing*, vol. 335, pp. 9–20, 2019, doi: 10.1016/j.neucom.2019.01.048.
- [9] X. Bai, Y. Zhang, F. Zhou, and B. Xue, "Quadtree-based multi-focus image fusion using a weighted focus-measure," *Inf. Fusion*, vol. 22, pp. 105–118, 2015, doi: 10.1016/j.inffus.2014.05.003.
- [10] Y. Zhang, X. Bai, and T. Wang, "Boundary finding based multi-focus image fusion through multi-scale morphological focus-measure," *Inf. Fusion*, vol. 35, pp. 81–101, 2017, doi: 10.1016/j.inffus.2016.09.006.
- [11] Y. Liu and Z. Wang, "Simultaneous image fusion and denoising with adaptive sparse representation," *IET Image Process.*, vol. 9, no. 5, pp. 347–357, 2015, doi: 10.1049/iet-ipr.2014.0311.
- [12] Y. Liu, X. Chen, R. K. Ward, Z. J. Wang, and S. Member, "Sparse Representation," *Comput. Vis.*, vol. 23, no. 12, pp. 748–748, 2014, doi: 10.1007/978-0-387-31439-6\_100096.
- [13] M. Amin-Naji and A. Aghagolzadeh, "Multi-Focus Image Fusion in DCT Domain using Variance and Energy of Laplacian and Correlation Coefficient for Visual Sensor Networks," *J. AI Data Min.*, vol. 6, no. 2, pp. 233–250, 2018, doi: 10.22044/JADM.2017.5169.1624.
- [14] W. Z. Liu Yu, "Multi-focus image fusion based on wavelet transform and adaptive block," *J. image Graph.*, vol. 8, no. 11, pp. 1435–1444, 2013.
- [15] S. Li, X. Kang, and J. Hu, "Image fusion with guided filtering," *IEEE Trans. Image Process.*, vol. 22, no. 7, pp. 2864–2875, 2013, doi: 10.1109/TIP.2013.2244222.
- [16] D. P. Bavarisetti, G. Xiao, J. Zhao, R. Dhuli, and G. Liu, "Multi-scale Guided Image and Video Fusion: A Fast and Efficient Approach," *Circuits, Syst. Signal Process.*, vol. 38, no. 12, pp. 5576–5605, 2019, doi: 10.1007/s00034-019-01131-z.
- [17] M. Amin-Naji, P. Ranjbar-Noiey, and A. Aghagolzadeh, "Multi-focus image fusion using Singular Value Decomposition in DCT domain," *Iran. Conf. Mach. Vis. Image Process. MVIP*, vol. 2017-November, pp. 45–51, 2018, doi: 10.1109/IranianMVIP.2017.8342367.
- [18] S. Paul, I. S. Sevcenco, and P. Agathoklis, "Multi-exposure and multi-focus image fusion in gradient domain," *J. Circuits, Syst. Comput.*, vol. 25, no. 10, pp. 1–18, 2016, doi: 10.1142/S0218126616501231.
- [19] Z. Zhou, S. Li, and B. Wang, "Multi-scale weighted gradient-based fusion for multi-focus images," *Inf. Fusion*, vol. 20, no. 1, pp. 60–72, 2014, doi: 10.1016/j.inffus.2013.11.005.
- [20] H. Li, L. Li, and J. Zhang, "Multi-focus image fusion based on sparse feature matrix decomposition and morphological filtering," *Opt. Commun.*, vol. 342, pp. 1–11, 2015, doi: 10.1016/j.optcom.2014.12.048.
- [21] Y. Liu, S. Liu, and Z. Wang, "A general framework for image fusion based on multi-scale transform and sparse representation," *Inf. Fusion*, vol. 24, pp. 147–164, 2015, doi: 10.1016/j.inffus.2014.09.004.
- [22] Y. Liu, X. Chen, H. Peng, and Z. Wang, "Multi-focus image fusion with a deep convolutional neural network," *Inf. Fusion*, vol. 36, pp. 191–207, 2017, doi: 10.1016/j.inffus.2016.12.001.
- [23] J. Li et al., "DRPL: Deep Regression Pair Learning for Multi-Focus Image Fusion," *IEEE Trans. Image Process.*, vol. 29, pp. 4816–4831, 2020, doi: 10.1109/TIP.2020.2976190.
- [24] M. Amin-Naji, A. Aghagolzadeh, and M. Ezoji, "Ensemble of CNN for multi-focus image fusion," *Inf. Fusion*, vol. 51, no. August 2018, pp. 201–214, 2019, doi: 10.1016/j.inffus.2019.02.003.
- [25] Y. Zhang, Y. Liu, P. Sun, H. Yan, X. Zhao, and L. Zhang, "IFCNN: A general image fusion framework based on convolutional neural network," *Inf. Fusion*, vol. 54, no. August 2018, pp. 99–118, 2020, doi: 10.1016/j.inffus.2019.07.011.
- [26] R. Lai, Y. Li, J. Guan, and A. Xiong, "Multi-Scale Visual Attention Deep Convolutional Neural Network for Multi-Focus Image Fusion," *IEEE Access*, vol. 7, pp. 114385–114399, 2019, doi: 10.1109/ACCESS.2019.2935006.
- [27] X. Song and X. W. B, *Multimodal Pattern Recognition of Social Signals in Human-Computer-Interaction - 5th {IAPR} {TC} 9 Workshop, {MPRSS} 2018, Beijing, China, August 20, 2018, Revised Selected Papers*, vol. 11377. Springer International Publishing, 2019.

- [28] H. Xu, J. Ma, Z. Le, J. Jiang, and X. Guo, "FusionDN: A unified densely connected network for image fusion," AAAI 2020 - 34th AAAI Conf. Artif. Intell., pp. 12484–12491, 2020, doi: 10.1609/aaai.v34i07.6936.
- [29] H. Xu, F. Fan, H. Zhang, Z. Le, and J. Huang, "A Deep Model for Multi-Focus Image Fusion Based on Gradients and Connected Regions," IEEE Access, vol. 8, pp. 26316–26327, 2020, doi: 10.1109/ACCESS.2020.2971137.
- [30] B. Ma, Y. Zhu, X. Yin, X. Ban, H. Huang, and M. Mukeshimana, "SESF-Fuse: an unsupervised deep model for multi-focus image fusion," Neural Comput. Appl., vol. 33, no. 11, pp. 5793–5804, 2021, doi: 10.1007/s00521-020-05358-9.
- [31] H. Zhang, H. Xu, Y. Xiao, X. Guo, and J. Ma, "Rethinking the Image Fusion : A Fast Unified Image Fusion Network based on Proportional Maintenance of Gradient and Intensity," 2020.
- [32] H. Xu, J. Ma, J. Jiang, X. Guo, and H. Ling, "U2Fusion: A Unified Unsupervised Image Fusion Network," IEEE Trans. Pattern Anal. Mach. Intell., vol. 8828, no. c, pp. 1–1, 2020, doi: 10.1109/tpami.2020.3012548.
- [33] M. D. Zeiler, D. Krishnan, G. W. Taylor, and R. Fergus, "Deconvolutional networks," Proc. IEEE Comput. Soc. Conf. Comput. Vis. Pattern Recognit., pp. 2528–2535, 2010, doi: 10.1109/CVPR.2010.5539957.
- [34] F. B. M. Suah, "Preparation and characterization of a novel Co(II) optode based on polymer inclusion membrane," Anal. Chem. Res., vol. 12, pp. 40–46, 2017, doi: 10.1016/j.ancr.2017.02.001.
- [35] W. Shi et al., "Real-Time Single Image and Video Super-Resolution Using an Efficient Sub-Pixel Convolutional Neural Network," Proc. IEEE Comput. Soc. Conf. Comput. Vis. Pattern Recognit., vol. 2016-December, pp. 1874–1883, 2016, doi: 10.1109/CVPR.2016.207.
- [36] X. Hu, H. Mu, X. Zhang, Z. Wang, T. Tan, and J. Sun, "Meta-SR: A magnification-arbitrary network for super-resolution," Proc. IEEE Comput. Soc. Conf. Comput. Vis. Pattern Recognit., vol. 2019-June, pp. 1575–1584, 2019, doi: 10.1109/CVPR.2019.00167.
- [37] G. Freedman and R. Fattal, "Image and video upscaling from local self-examples," ACM Trans. Graph., vol. 30, no. 2, 2011, doi: 10.1145/1944846.1944852.
- [38] C. Y. Yang, J. Bin Huang, and M. H. Yang, "Exploiting self-similarities for single frame super-resolution," Lect. Notes Comput. Sci. (including Subser. Lect. Notes Artif. Intell. Lect. Notes Bioinformatics), vol. 6494 LNCS, no. PART 3, pp. 497–510, 2011, doi: 10.1007/978-3-642-19318-7\_39.
- [39] D. Glasner, S. Bagon, and M. Irani, "Super-resolution from a single image," Proc. IEEE Int. Conf. Comput. Vis., no. Iccv, pp. 349–356, 2009, doi: 10.1109/ICCV.2009.5459271.
- [40] K. I. Kim and Y. Kwon, "Single-image super-resolution using sparse regression and natural image prior," IEEE Trans. Pattern Anal. Mach. Intell., vol. 32, no. 6, pp. 1127–1133, 2010, doi: 10.1109/TPAMI.2010.25.
- [41] C. Dong, C. C. Loy, K. He, and X. Tang, "Image Super-Resolution Using Deep Convolutional Networks," IEEE Trans. Pattern Anal. Mach. Intell., vol. 38, no. 2, pp. 295–307, 2016, doi: 10.1109/TPAMI.2015.2439281.
- [42] J. Kim, J. K. Lee, and K. M. Lee, "Deeply-recursive convolutional network for image super-resolution," Proc. IEEE Comput. Soc. Conf. Comput. Vis. Pattern Recognit., vol. 2016-December, pp. 1637–1645, 2016, doi: 10.1109/CVPR.2016.181.
- [43] W. S. Lai, J. Bin Huang, N. Ahuja, and M. H. Yang, "Deep laplacian pyramid networks for fast and accurate super-resolution," Proc. - 30th IEEE Conf. Comput. Vis. Pattern Recognition, CVPR 2017, vol. 2017-January, pp. 5835–5843, 2017, doi: 10.1109/CVPR.2017.618.
- [44] C. Ledig et al., "Photo-realistic single image super-resolution using a generative adversarial network," Proc. - 30th IEEE Conf. Comput. Vis. Pattern Recognition, CVPR 2017, vol. 2017-January, pp. 105–114, 2017, doi: 10.1109/CVPR.2017.19.
- [45] B. Lim, S. Son, H. Kim, S. Nah, and K. M. Lee, "Enhanced Deep Residual Networks for Single Image Super-Resolution," IEEE Comput. Soc. Conf. Comput. Vis. Pattern Recognit. Work., vol. 2017-July, pp. 1132–1140, 2017, doi: 10.1109/CVPRW.2017.151.
- [46] Y. Zhang, Y. Tian, Y. Kong, B. Zhong, and Y. Fu, "Residual Dense Network for Image Super-Resolution," Proc. IEEE Comput. Soc. Conf. Comput. Vis. Pattern Recognit., pp. 2472–2481, 2018, doi: 10.1109/CVPR.2018.00262.
- [47] W. Han, S. Chang, D. Liu, M. Yu, M. Witbrock, and T. S. Huang, "Image Super-Resolution via Dual-State Recurrent Networks," Proc. IEEE Comput. Soc. Conf. Comput. Vis. Pattern Recognit., pp. 1654–1663, 2018, doi: 10.1109/CVPR.2018.00178.
- [48] Y. LeCun, L. Bottou, Y. Bengio, and P. Haffner, "Gradient-based learning applied to document recognition," Proc. IEEE, vol. 86, no. 11, pp. 2278–2323, 1998, doi: 10.1109/5.726791.

- [49] T. F. Gonzalez, "Handbook of approximation algorithms and metaheuristics," *Handb. Approx. Algorithms Metaheuristics*, pp. 1–1432, 2007, doi: 10.1201/9781420010749.
- [50] K. Simonyan and A. Zisserman, "Very deep convolutional networks for large-scale image recognition," *3rd Int. Conf. Learn. Represent. ICLR 2015 - Conf. Track Proc.*, pp. 1–14, 2015.
- [51] C. Szegedy et al., "Going deeper with convolutions," *Proc. IEEE Comput. Soc. Conf. Comput. Vis. Pattern Recognit.*, vol. 07-12-June-2015, pp. 1–9, 2015, doi: 10.1109/CVPR.2015.7298594.
- [52] J. Kim, J. K. Lee, and K. M. Lee, "Accurate image super-resolution using very deep convolutional networks," *Proc. IEEE Comput. Soc. Conf. Comput. Vis. Pattern Recognit.*, vol. 2016-December, pp. 1646–1654, 2016, doi: 10.1109/CVPR.2016.182.
- [53] K. He, X. Zhang, S. Ren, and J. Sun, "Deep residual learning for image recognition," *Proc. IEEE Comput. Soc. Conf. Comput. Vis. Pattern Recognit.*, vol. 2016-December, pp. 770–778, 2016, doi: 10.1109/CVPR.2016.90.
- [54] G. Huang, Z. Liu, L. Van Der Maaten, and K. Q. Weinberger, "Densely connected convolutional networks," *Proc. - 30th IEEE Conf. Comput. Vis. Pattern Recognition, CVPR 2017*, vol. 2017-January, pp. 2261–2269, 2017, doi: 10.1109/CVPR.2017.243.
- [55] Z. Wang, J. Chen, and S. C. H. Hoi, "Deep Learning for Image Super-Resolution : A Survey," vol. 43, no. 10, pp. 3365–3387, 2021.
- [56] Y. Tan et al., "CrossNet++: Cross-scale Large-parallax Warping for Reference-based Super-resolution," *IEEE Trans. Pattern Anal. Mach. Intell.*, vol. 8828, no. c, pp. 1–1, 2020, doi: 10.1109/tpami.2020.2997007.
- [57] Y. Wang, F. Perazzi, B. McWilliams, A. Sorkine-Hornung, O. Sorkine-Hornung, and C. Schroers, "A fully progressive approach to single-image super-resolution," *IEEE Comput. Soc. Conf. Comput. Vis. Pattern Recognit. Work.*, vol. 2018-June, pp. 977–986, 2018, doi: 10.1109/CVPRW.2018.00131.
- [58] M. Haris, G. Shakhnarovich, and N. Ukita, "Deep Back-Projection Networks for Single Image Super-resolution," *IEEE Trans. Pattern Anal. Mach. Intell.*, vol. 2, no. d, pp. 1–1, 2020, doi: 10.1109/tpami.2020.3002836.
- [59] Z. Li, J. Yang, Z. Liu, X. Yang, G. Jeon, and W. Wu, "Feedback network for image super-resolution," *Proc. IEEE Comput. Soc. Conf. Comput. Vis. Pattern Recognit.*, vol. 2019-June, pp. 3862–3871, 2019, doi: 10.1109/CVPR.2019.00399.
- [60] J. Ai, G. Fan, Y. Mao, J. Jin, M. Xing, and H. Yan, "An Improved SRGAN Based Ambiguity Suppression Algorithm for SAR Ship Target Contrast Enhancement," *IEEE Geosci. Remote Sens. Lett.*, pp. 1–5, 2021, doi: 10.1109/LGRS.2021.3111553.
- [61] H. Wang, "HFD - SRGAN : Super-Resolution Generative Adversarial Network with High-frequency discriminator," pp. 3148–3153, 2020.
- [62] M. M. Majdabadi and S. B. Ko, "MSG-CapsGAN: Multi-Scale Gradient Capsule GAN for Face Super Resolution," *2020 Int. Conf. Electron. Information, Commun. ICEIC 2020*, pp. 10–12, 2020, doi: 10.1109/ICEIC49074.2020.9051244.
- [63] A. Mahendran and A. Vedaldi, "Understanding deep image representations by inverting them," *Proc. IEEE Comput. Soc. Conf. Comput. Vis. Pattern Recognit.*, vol. 07-12-June-2015, pp. 5188–5196, 2015, doi: 10.1109/CVPR.2015.7299155.
- [64] V. Lempitsky, A. Vedaldi, and D. Ulyanov, "Deep Image Prior," *Proc. IEEE Comput. Soc. Conf. Comput. Vis. Pattern Recognit.*, pp. 9446–9454, 2018, doi: 10.1109/CVPR.2018.00984.
- [65] N. Navab, J. Hornegger, W. M. Wells, and A. F. Frangi, "Medical Image Computing and Computer-Assisted Intervention - MICCAI 2015: 18th International Conference Munich, Germany, October 5-9, 2015 proceedings, part III," *Lect. Notes Comput. Sci. (including Subser. Lect. Notes Artif. Intell. Lect. Notes Bioinformatics)*, vol. 9351, no. Cvd, pp. 12–20, 2015, doi: 10.1007/978-3-319-24574-4.
- [66] Y. Gandelsman, A. Shocher, and M. Irani, "'Double-dip': Unsupervised image decomposition via coupled deep-image-priors," *Proc. IEEE Comput. Soc. Conf. Comput. Vis. Pattern Recognit.*, vol. 2019-June, no. 788535, pp. 11018–11027, 2019, doi: 10.1109/CVPR.2019.01128.
- [67] M. Nejati, S. Samavi, and S. Shirani, "Multi-focus image fusion using dictionary-based sparse representation," *Inf. Fusion*, vol. 25, pp. 72–84, 2015, doi: 10.1016/j.inffus.2014.10.004.
- [68] H. Zhao, O. Gallo, I. Frosio, and J. Kautz, "Loss Functions for Image Restoration with Neural Networks," pp. 1–11.
- [69] V. Baroncini, L. Capodiferro, E. D. Di Claudio, and G. Jacovitti, "The polar edge coherence: A quasi blind metric for video quality assessment," *Eur. Signal Process. Conf.*, no. September, pp. 564–568, 2009.